

## Article

# Ruthenium and Nickel Molybdate-Decorated 2D Porous Graphitic Carbon Nitrides for Highly Sensitive Cardiac Troponin Biosensor

Walaa Khushaim <sup>1</sup>, Veerappan Mani <sup>1</sup> , Karthik Peramaiya <sup>2</sup>, Kuo-Wei Huang <sup>2</sup> and Khaled Nabil Salama <sup>1,\*</sup> 

<sup>1</sup> Sensors Lab, Advanced Membranes and Porous Materials Center, Computer, Electrical and Mathematical Science and Engineering Division, King Abdullah University of Science and Technology (KAUST), Thuwal 23955-6900, Saudi Arabia

<sup>2</sup> KAUST Catalysis Center and Physical Science and Engineering Division, King Abdullah University of Science and Technology (KAUST), Thuwal 23955-6900, Saudi Arabia

\* Correspondence: khaled.salama@kaust.edu.sa

**Abstract:** Two-dimensional (2D) layered materials functionalized with monometallic or bimetallic dopants are excellent materials to fabricate clinically useful biosensors. Herein, we report the synthesis of ruthenium nanoparticles (RuNPs) and nickel molybdate nanorods (NiMoO<sub>4</sub> NRs) functionalized porous graphitic carbon nitrides (PCN) for the fabrication of sensitive and selective biosensors for cardiac troponin I (cTn-I). A wet chemical synthesis route was designed to synthesize PCN-RuNPs and PCN-NiMoO<sub>4</sub> NRs. Morphological, elemental, spectroscopic, and electrochemical investigations confirmed the successful formation of these materials. PCN-RuNPs and PCN-NiMoO<sub>4</sub> NRs interfaces showed significantly enhanced electrochemically active surface areas, abundant sites for immobilizing bioreceptors, porosity, and excellent aptamer capturing capacity. Both PCN-RuNPs and PCN-NiMoO<sub>4</sub> NRs materials were used to develop cTn-I sensitive biosensors, which showed a working range of 0.1–10,000 ng/mL and LODs of 70.0 pg/mL and 50.0 pg/mL, respectively. In addition, the biosensors were highly selective and practically applicable. The functionalized 2D PCN materials are thus potential candidates to develop biosensors for detecting acute myocardial infarctions.

**Keywords:** two-dimensional materials; nickel molybdate; ruthenium nanoparticles; cardiac troponin; aptasensor



**Citation:** Khushaim, W.; Mani, V.; Peramaiya, K.; Huang, K.-W.; Salama, K.N. Ruthenium and Nickel Molybdate-Decorated 2D Porous Graphitic Carbon Nitrides for Highly Sensitive Cardiac Troponin Biosensor. *Biosensors* **2022**, *12*, 783. <https://doi.org/10.3390/bios12100783>

Received: 14 August 2022

Accepted: 19 September 2022

Published: 22 September 2022

**Publisher's Note:** MDPI stays neutral with regard to jurisdictional claims in published maps and institutional affiliations.



**Copyright:** © 2022 by the authors. Licensee MDPI, Basel, Switzerland. This article is an open access article distributed under the terms and conditions of the Creative Commons Attribution (CC BY) license (<https://creativecommons.org/licenses/by/4.0/>).

## 1. Introduction

Cardiovascular disease (CVD) is the most prevalent chronic disease worldwide, accounting for 17.3 million deaths per year across the globe, projected to grow to over 23.6 million deaths per year by 2030 [1,2]. CVD is a major public health concern and imposes a huge economic burden on people and governments. Cardiac troponin (cTn-I) is the most promising biomarker for CVD, and cTn-I biosensors are employed for the clinical diagnosis of CVD [3]. As the ranges of cTn-I levels in serum are in the pg/mL level, functional nanomaterials, which enhance the sensitivity and detection ranges of cTn-I biosensors, are needed to increase their performance [4,5].

Two-dimensional layered materials are outstanding materials for biosensing applications, mainly because of their large surface areas, conductivity, catalytic sites, solution processability, and ease of synthesis and functionalization [6–9]. Graphitic carbon nitride nanosheets (GCN) are emerging 2D materials known for their distinctive properties, such as defect sites, edge densities, nitrogen lone pairs, and pi-densities [10–12]. Porous graphitic carbon nitride (PCN) is the derivative of GCN installed with significant porous structures and altered electronic structures [13]. The surface area, structural N defect densities, and the number of surface-active sites—all crucial characteristics of a material to be exploited in biosensing applications—are increased by the existence of a porous structure [14,15].

Most importantly, the porous structures provide a high level of flexibility to the material, which enable an increased adaptability and stability of the bio-receptors that are attached to them [16,17]. Recent research showed that PCN outperforms GCN and provides a 2.8-fold increased hydrogen evolution efficiency because of the added porosity of the 2D layers [18]. PCN conductivity and aptamer immobilizing characteristics can be further improved by decorating the PCN surface with metal nanoparticles [19,20].

Ru nanoparticles (RuNPs) are interesting materials known for their excellent electrocatalytic properties [21]. Recent studies found that RuNPs exhibit a peroxidase-like behavior and they could be used as potential materials to fabricate biosensors [22]. Ru-based binary or multi-metallic NPs are employed in electrochemical sensors because of their distinctive electrocatalytic properties, better surface area-to-volume ratios, and synergistic effects [23]. Combining a porous support with RuNPs not only stabilizes the NPs but also enables synergistic properties; PCN-RuNPs have never been used in biosensing applications. Nickel molybdate ( $\text{NiMoO}_4$ ) is a binary metal oxide which provides improved redox properties of Ni and Mo for electrochemical applications [24]. Mo sites have a unique chemical affinity for thiolated aptamer linkers, bound via van der Waals force. Furthermore, the Ni and Mo atoms are well-known for their multiple redox characteristics which are useful to mediate electron transfer reactions between aptamers and electrode surfaces.

The objective of this work was to develop a sensitive cTn-I sensing system, using RuNPs and  $\text{NiMoO}_4$  nanoparticle-functionalized PCN materials. First, PCN was prepared from GCN through a simple acid-treatment. Next, RuNPs and  $\text{NiMoO}_4$  NRs-functionalized PCN materials were synthesized by subsequent chemical/hydrothermal treatments (Figure 1). Following that, these materials were employed to modify the working electrodes of laser-scribed graphene electrodes, which were later immobilized with cTn-I-specific thiol-functionalized aptamers to construct a cTn-I biosensor. Our investigations found that PCN-based 2D materials are excellent candidates to develop biosensors for cardiac biomarkers. The advantages of the described synthetic method are the simple and straightforward synthetic procedures, the use of melamine as a low-cost precursor, and the use of inexpensive synthesis instruments.

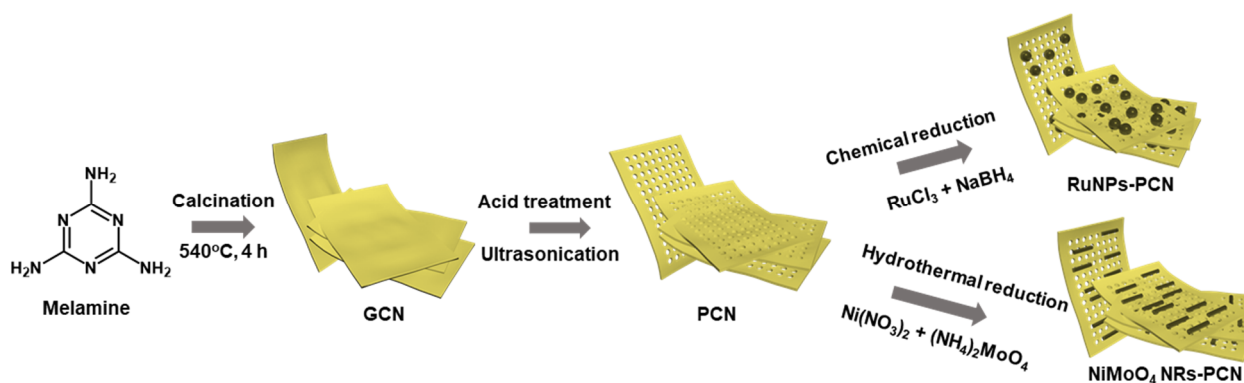


**Figure 1.** Synthesis of PCN-RuNPs and PCN- $\text{NiMoO}_4$  NRs.

## 2. Experimental

### 2.1. Chemicals and Apparatus

A thiolated aptamer consisting of the DNA sequence CGTGCAGTACGCCAACCTTTCTCATGCG CTGCCCTCTTA, developed previously by Jo et al., was purchased from Sigma and used in this work [25]. 100  $\mu\text{M}$  aptamer stock solution was prepared and stored at  $-20^\circ\text{C}$ . A stock solution of 200  $\mu\text{M}$  mercaptohexanol (MCH) was prepared in 0.01 M PBS. Myoglobin (Myo), cardiac troponin I (cTn-I), cardiac troponin T (cTn-T), and cardiac troponin C (cTn-C) were bought from Abcam (Cambridge, UK). H4522 human serum was purchased from Sigma. Scanning electron microscopy (SEM) studies were performed using Zeiss Merlin and TeneoVS field-emission scanning electron microscopes. Transmission electron microscopy (TEM) experiments were conducted using the FEI Themis

Z instrument (Thermo Fisher Scientific, Massachusetts, United States). XRD patterns were performed using Bruker X-ray diffraction (XRD) D8 advance equipment (Karlsruhe, Germany). AMICUS X-ray photoelectron spectroscopy (XPS) apparatus from Kratos Analytical (Manchester, UK) was used for the XPS analysis. A multiEmStat3-PalmSens electrochemical workstation was used for the electrochemical studies. Polyimide (PI) substrates were bought from Utech Products (New York, NY, USA). For laser patterning, a CO<sub>2</sub> laser from Universal Laser Systems® PLS6.75 with a 150 m laser spot diameter and a 10.6 m wavelength was used [26,27]. A three-electrode system with diameters of 2.8 cm, 1.2 cm, and 1.5 mm was patterned onto a pre-cleaned PI sheet. To prepare laser-scribed graphene electrodes (LSGEs) with a relatively low sheet resistance (58/square), the following ideal parameters were used: 3.2 W power, 2.8 cm/s speed, 1000 pulses per inch, and 2.5 mm Z distance [28]. The electrochemical cell was a three-electrode chip system, with the reference and counter electrodes being laser-scribed graphene electrodes and the working electrode being either RuNPs-PCN or NiMoO<sub>4</sub> NRs-PCN. An electrode connector was used to link the chips to the PalmSens electrochemical workstation. The cell volume was 75 µL.

## 2.2. Nanomaterials Synthesis

Figure 1 shows the synthesis of GCN, PCN, RuNPs-PCN, and NiMoO<sub>4</sub> NRs-PCN. First, using a standard thermal polymerization technique, GCN was made from melamine. A GCN powder was produced by calcining 2 g of melamine at 540 °C for 4 h at a rate of 5 °C/min. The color of the powder changed from white to yellow, signifying the formation of GCN. The GCN powder was washed three times in water and three times in ethanol, and then dried at 50 °C overnight. Next, an acid treatment was implemented to prepare PCN from GCN. About 250 mg of GCN powder was added to 30 mL H<sub>2</sub>SO<sub>4</sub>, and subsequent ultrasonic agitation was performed for 15 min. The mixture was then continually agitated with a magnetic stirrer until the color of the solution changed from yellow to colorless. Finally, 100 mL of ice-cold water was added to the reaction media, producing white-colored flakes. The resulting flakes were centrifuged, washed three times with water and three times with ethanol, and then dried at 50 °C overnight.

A typical chemical reduction method was adopted to deposit RuNPs onto the PCN surface. About 0.50 g of PCN was dispersed in 50 mL water. RuCl<sub>3</sub> was then added and agitated for 15 min. The mixture was then agitated for an additional 1 h after 10 mL of 0.1 M NaBH<sub>4</sub> solution was added. RuNPs-PCN nanomaterial was produced by centrifuging the final product, washing it three times with water and three times with ethanol, and then freeze-drying it for an entire night. Next, NiMoO<sub>4</sub> NRs-PCN nanomaterial was prepared using a hydrothermal procedure. About 0.50 g of PCN was dispersed in 50 mL of water. Then 2 mM nickel nitrate and ammonium molybdate were added to the PCN solution and the whole mixture (70 mL) was transferred to a Teflon-lined autoclave and treated hydrothermally at 170 °C for 4 h. The product was separated, washed with water and ethanol, and freeze-dried overnight, yielding NiMoO<sub>4</sub> NRs-PCN.

## 2.3. Biosensor Fabrication Steps and Analysis Procedure

About 2 mg/mL of RuNPs-PCN or NiMoO<sub>4</sub> NRs-PCN aqueous solutions were prepared by ultrasonically treating the respective dispersion for 15 min. About 5.0 µL of RuNPs-PCN or NiMoO<sub>4</sub> NRs-PCN was dropped onto the working electrode of the LSGE and dried. The resulting electrodes were either RuNPs-PCN/LSGE or NiMoO<sub>4</sub> NRs-PCN/LSGE. Next, the nanomaterial-modified electrodes were used to fabricate the cTn-I aptasensor, which is schematically presented in Figure 2. First, a mixture of 8.0 µM (optimized) cTn-I aptamer and 20 µM MCH was prepared in 10 mM PBS (pH 7.4). About 6.0 µL aptamer-MCH mixture was drop-casted onto the working electrode of the modified LSGEs and incubated for 12 h. The modified electrode was then washed with PBS three times. To prevent non-specific sites, the electrode was then incubated with 0.10 mg/mL BSA for 20 min. The resulting devices were either an RuNPs-PCN/LSGE aptasensor or an NiMoO<sub>4</sub> NRs-PCN/LSGE aptasensor. First, desired quantities of cTn-I were produced in 10 mM PBS

for cTn-I analysis. Then, 10  $\mu\text{L}$  of cTn-I was placed on the working electrodes and incubated for 30 min. The electrodes were then cleaned three times with 0.01 M PBS (pH 7.40) to get rid of the unbound analytes. For real sample analysis, cTn-I-spiked human serum samples were used. 10  $\mu\text{L}$  of serum sample was dropped onto the working electrode, incubated for 30 min, washed with PBS, and then analyzed using either the RuNPs-PCN/LSGE aptasensor or the NiMoO<sub>4</sub> NRs-PCN/LSGE aptasensor.

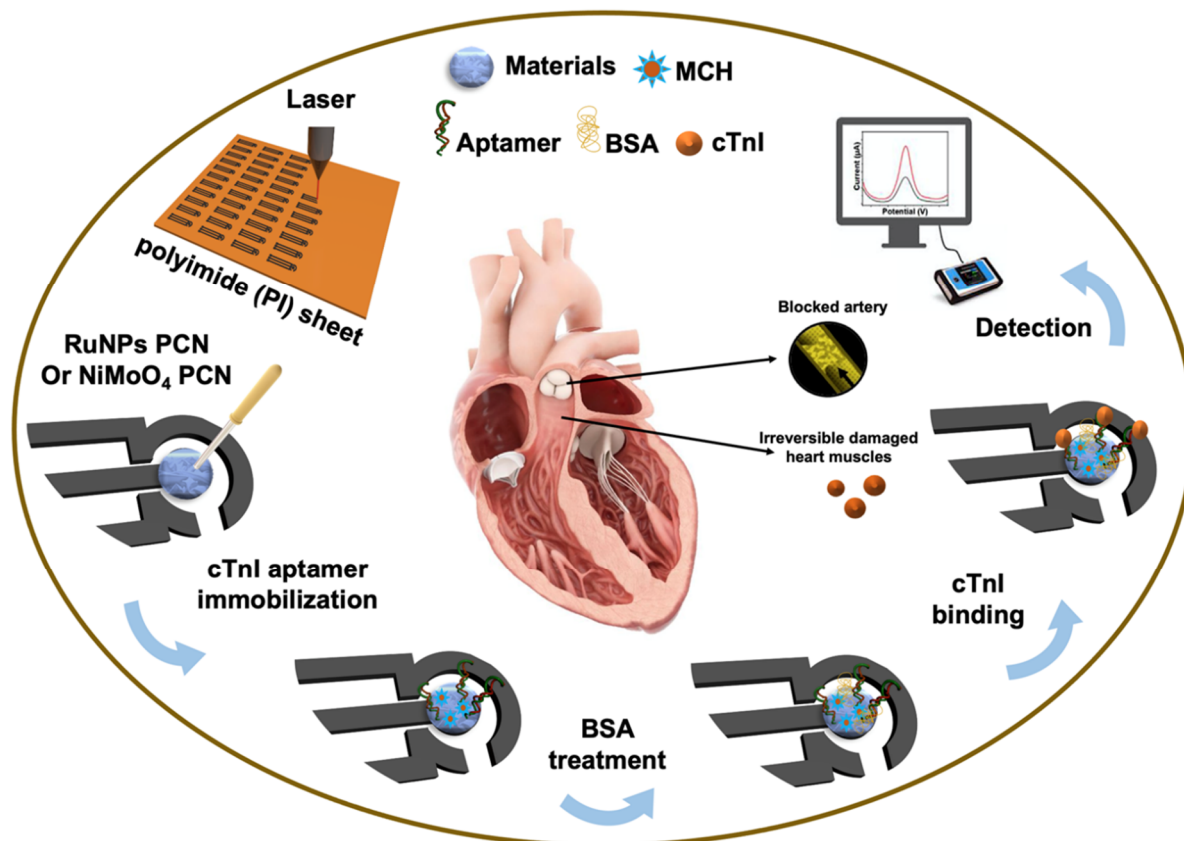


**Figure 2.** Schematic illustration for the fabrication of the RuNPs-PCN/LSGE aptasensor or the NiMoO<sub>4</sub> NRs-PCN/LSGE aptasensor.

#### 2.4. Electrochemical Assay Conditions

Cyclic voltammetry (CV) experiments were conducted in a potential range of  $-0.40$  V to  $+0.40$  V and a scan rate of  $0.05$  V/s, unless otherwise specified separately in the figure captions. Squarewave voltammetry (SWV) studies were carried out with a 2 Hz frequency and 0.10 V amplitude. Electrochemical impedance spectroscopy (EIS) analysis was used with a frequency range of 1.0 Hz–100 kHz, an amplitude of 0 V, and a bias potential of 5.0 mV. The calibration plots were prepared using normalized current, which was determined by subtracting the peak currents of the redox probe before and after cTn-I binding. All the electrochemical experiments were conducted in 0.10 M KCl containing a mixture of 5.0 mM K<sub>3</sub>/K<sub>4</sub>[Fe(CN)<sub>6</sub>]. All measurements were repeated at least three times and the average was used to prepare data.

### 3. Results and Discussions

#### 3.1. Characterizations

The TEM analysis of the PCN-RuNPs showed a large number of porous structures with a distribution of ultrafine Ru nanoparticles (Figure 3A,B). The particle size of Ru was in the range of 1–3 nm. The XRD pattern of PCN-RuNPs showed the typical crystal characteristic of carbon nitride (Figure 3C). PCN crystal structure was confirmed by two

prominent peaks observed at  $3.3^\circ$  and  $27.0^\circ$ , which were associated with (100) and (002) planes, respectively [29]. The XRD curve of PCN-RuNPs did not show any typical peaks of the Ru phase, which is likely due to the ultra-small particle size and high dispersion degree of RuNPs in the material. XPS was then used to analyze the surface electrical structure of the PCN-RuNPs (Figure 3D–G). The XPS survey spectrum showed signals that matched the elements C, N, and Ru. For the C 1s spectrum, moderately overlapped with the Ru 3d region, the divided peaks at 285.8, 284.8, 282.9, and 280.7 eV were assigned to N–C=N, C–C, Ru $^\circ$  3d $_{3/2}$ , and Ru $^\circ$  3d $_{5/2}$ , respectively. Two usual bands for Ru 3d $_{3/2}$  and Ru 3d $_{5/2}$  were also observed, consistent with previous reports [30]. The TEM image of PCN-NiMoO $_4$  NPs revealed the distribution of nanorod-shaped NiMoO $_4$  particles (Figure 4A). The nanorods were interconnected within the backbone of the PCN sheets (Figure 4B). The sheet-like structure of PCN was not evident in the TEM image because the NiMoO $_4$  structure darkened the PCN sheets. The crystal characteristic of the PCN phase and NiMoO $_4$  were perceived in the XRD pattern of PCN-NiMoO $_4$  NPs (Figure 4C). The XRD pattern is indexed in accordance with JCPDS file # 31-0902, which corresponds to the monoclinic phase of  $\alpha$ -NiMoO $_4$  [31]. In addition, characteristic PCN bands of  $13.4^\circ$  and  $27.8^\circ$  were identified. The XPS survey spectrum displayed the expected elements of C, N, O, Ni, and Mo in the composite (Figure 4D–J). The spectra of C 1S, N 1S, and O 1S were consistent with the corresponding pattern of PCN. The core-level spectrum of Ni 2p showed two key peaks at 856.5 and 878.7 eV, belonging to Ni 2p $_{3/2}$  and Ni 2p $_{1/2}$ , respectively, which are features of the Ni $^{2+}$  oxidation state. The deconvoluted Mo 3d core-level spectra had doublet peaks at 232.5 and 235.8 eV which corresponded to Mo 3d $_{5/2}$  and Mo 3d $_{3/2}$ , respectively, and showed that Mo was in the Mo $^{6+}$  state. In the O 1s binding energy spectrum, the peak at 530.5 eV represented metal–oxygen bonds. The Mo/Ni atomic ratio was found to be around 1:1.5, implying that some amorphous Ni may have co-existed in the structure [32].

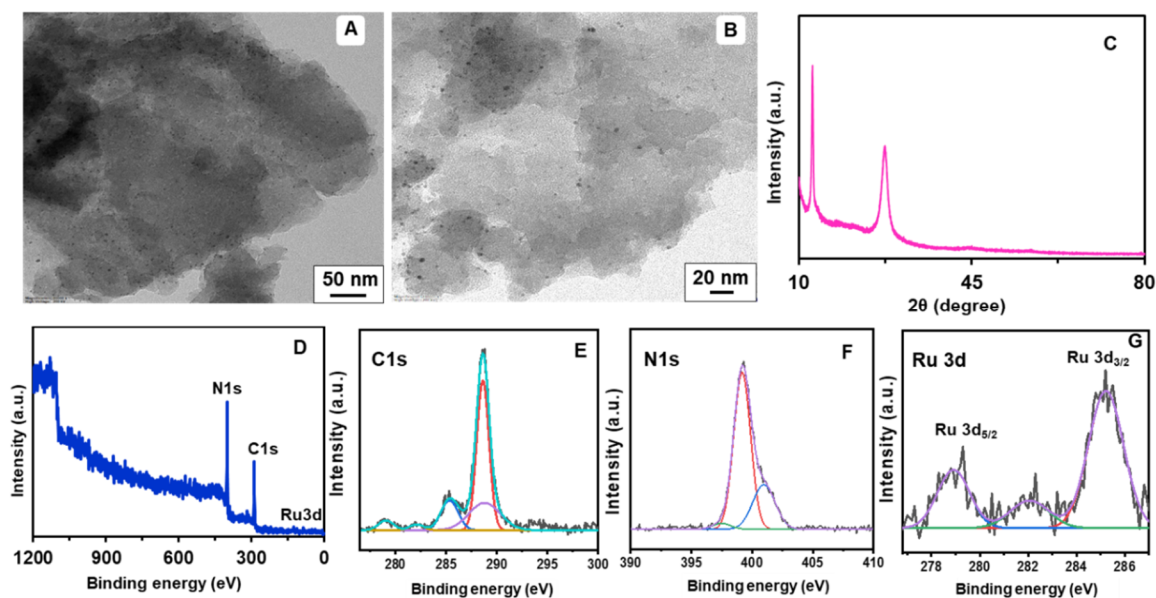


**Figure 3.** TEM images (A,B), XRD pattern (C), XPS survey spectrum (D), and XPS deconvoluted spectra (E–G) of PCN-RuNPs.

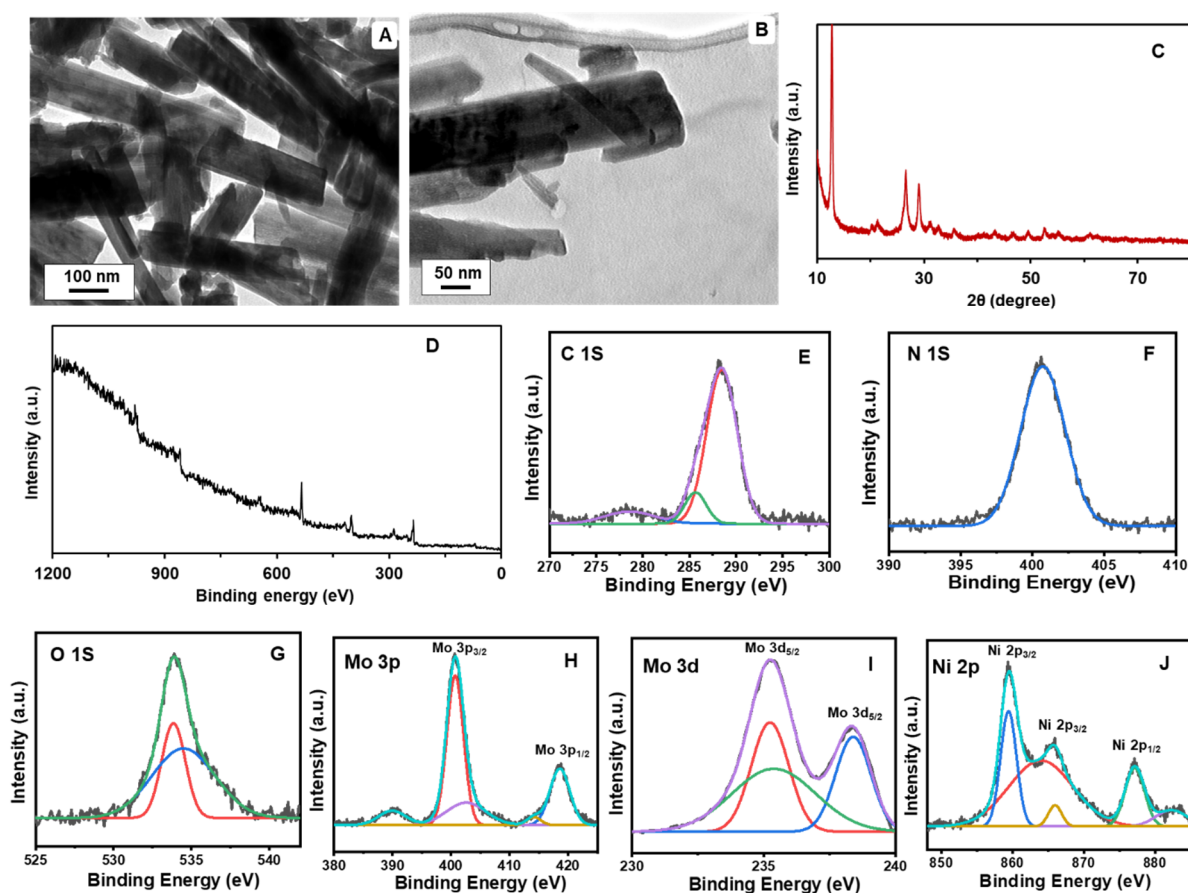


**Figure 4.** TEM images (A,B), XRD pattern (C), XPS survey spectrum (D), and deconvoluted XPS spectra (E–J) of PCN-NiMoO<sub>4</sub> NPs.

### 3.2. Electrochemically Active Surface Area

The electrochemical properties of the 2D nanomaterials were tested with the ferri/ferrocyanide redox model system (Figure 5A–C). The CVs of the PCN-RuNPs and PCN-NiMoO<sub>4</sub> NRs showed the typical redox couple of Fe<sup>2+</sup>/Fe<sup>3+</sup>. However, the kinetics of the redox process varied which is evident from the different slope values obtained in their kinetic plots (Figure 5D–F). Furthermore, the electrochemically active surface area (EASA) values of the electrodes were assessed by substituting the slope value of the kinetic plot into the repositioned Randles-Sevcik equation Equation (1),

$$= \frac{I_{pa}}{\sqrt{v}} \left[ \frac{1}{268600 n^3 D^{1/2} C} \right] \quad (1)$$

Here,  $A$  = electrochemical active surface area of the electrode,  $D$  = diffusion coefficient ( $6.70 \times 10^{-6} \text{ cm}^2 \cdot \text{s}^{-1}$ ),  $v$  = scan rate ( $\text{V} \cdot \text{s}^{-1}$ ),  $C$  = concentration of ferri/ferrocyanide solution ( $\text{mol} \cdot \text{cm}^{-3}$ ), and  $I_p$  = peak currents ( $\mu\text{A}$ ). The EASA values of PCN were also calculated for comparison.

The EASAs of the PCN-RuNPs, PCN-NiMoO<sub>4</sub> NRs, and PCN were estimated to be 0.0894, 0.0917, and 0.0872  $\text{cm}^2$ , respectively. The EASA trend follows the pattern of PCN-NiMoO<sub>4</sub> NPs > PCN-RuNPs > PCN. The values of the EASAs were significantly increased compared to their geometrical area. Both PCN-RuNPs and PCN-NiMoO<sub>4</sub> NRs showed an increase in performance compared to PCN. The considerable increase in the values of the EASA was because of the electrocatalytic properties of the RuNPs, NiMoO<sub>4</sub>, and PCN materials. The major contact between PCN materials and the LSGE surface was most likely

the result of a pi-stacking interaction between the triazine ring densities in PCN and the delocalized electrons in graphene sheets [33].

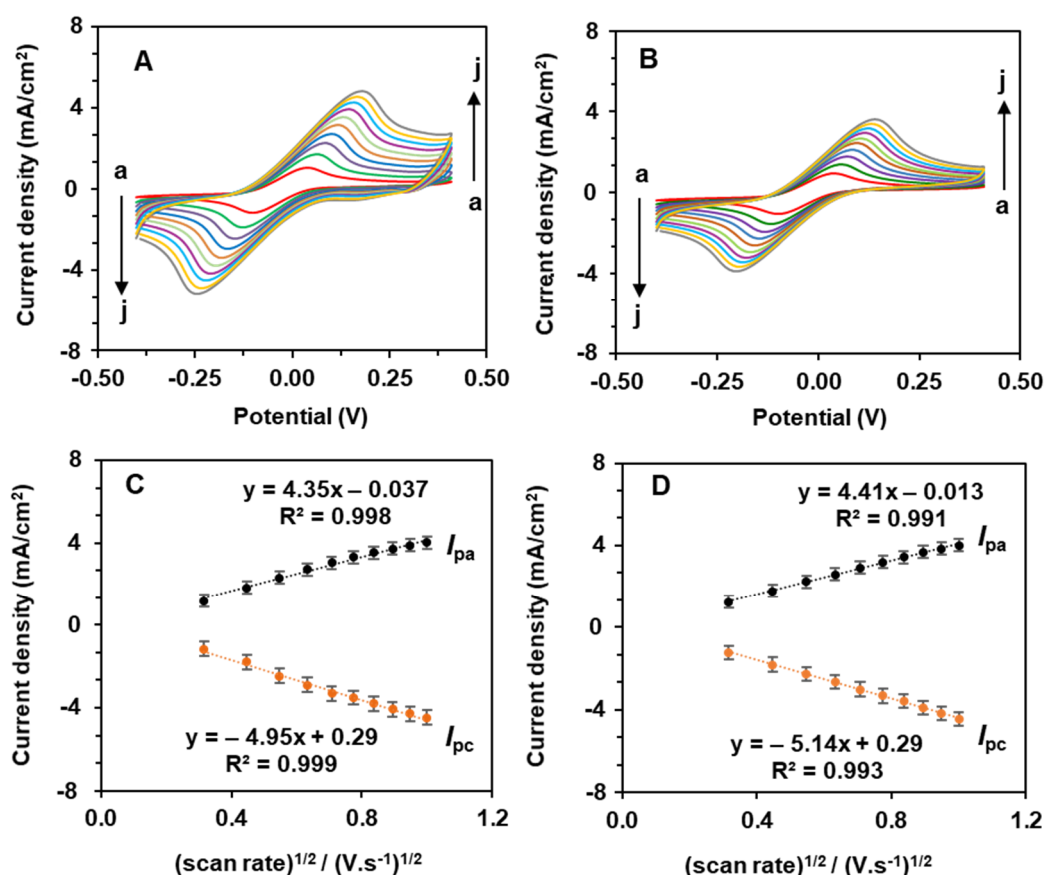


**Figure 5.** CVs for PCN-RuNPs (A) and PCN-NiMoO<sub>4</sub> NRs (B) modified LSGEs were obtained using 0.10 M KCl containing 5 mM K<sub>3</sub>/K<sub>4</sub>[Fe(CN)<sub>6</sub>] at various scan rates from 0.10 to 1.0 V/s (a to j). Peak currents for PCN-RuNPs (C) and PCN-NiMoO<sub>4</sub> NRs plotted against square root of scan rate (D).

### 3.3. Aptasensing Performances

Next, the biosensing aptitudes of the PCN-RuNPs and PCN-NiMoO<sub>4</sub> biosensors were tested. Figure 6 presents the CV, SWV, and EIS responses of the PCN-RuNPs aptasensors with and without cTn-I. The responses of the PCN-RuNPs material were also included for comparison. 10 ng/mL cTn-I elicited a significant decrease in the redox signals of the probe, indicating that the biosensor has the ability to sense cTn-I. The decrease was about 19.7% in CV and 16.2% in SWV. The decrease was because of the specific binding of the cTn-I with the recognition regions of its aptamer. This specific analyte-aptamer binding event inhibits the flow of electrons between Fe<sup>2+</sup>/Fe<sup>3+</sup> ions and the PCN-RuNPs/LSGE, which was revealed as a decreased signal in the current response. Evidently, the flow of electrons would be slowed down more rigorously if high concentrations of cTn-I are present, thus allowing a relationship between the concentration of the cTn-I and the normalized current signal of the redox probe. In addition to CV and SWV, EIS was used to further examine the sensor because EIS is a highly sensitive tool to look at changes in the interfacial electron transport. The charge transfer resistance of the PCN-RuNPs sensor was significantly increased in the presence of cTn-I. Apparently, the aptamer-cTn-I binding event increased the resistance for the interfacial electron transport caused between the aptamers and cTn-I, which resulted in the increased charge transfer resistance ( $R_{ct}$ ).

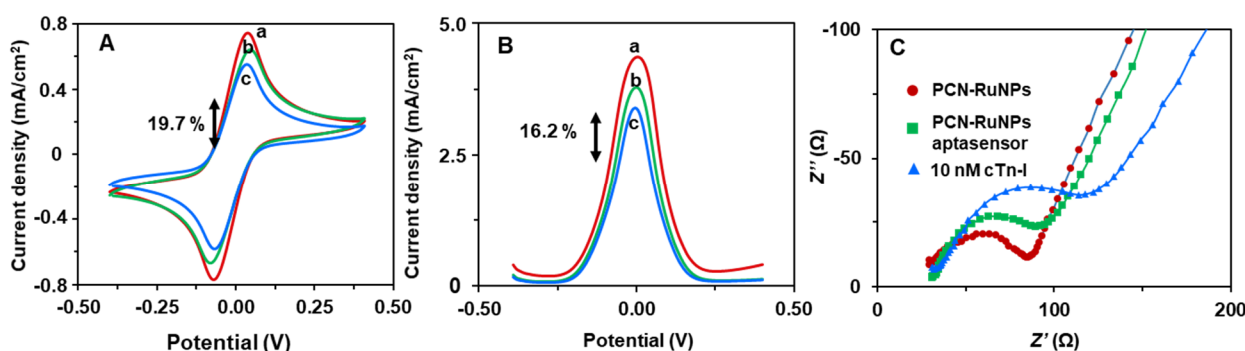


**Figure 6.** (A) CV, (B) SWV, and (C) EIS curves of PCN-RuNPs (a), PCN-RuNPs aptasensor (b), and PCN-RuNPs aptasensor + 10 ng/mL cTn-I (c). The supporting electrolyte 0.10 M KCl containing a mixture of 5.0 mM  $K_3/K_4[Fe(CN)_6]$ .

The sensing results of the PCN-NiMoO<sub>4</sub> aptasensor are similar to the PCN-RuNPs aptasensor, but the sensitivity is relatively higher for the PCN-NiMoO<sub>4</sub> NRs (Figure 7). The decrease is about 21.7% in CV and 15.6% in SWV. Because the NiMoO<sub>4</sub> has a relatively excessive EASA, edge densities, and redox properties originated from the advantage of having a binary composition of metal oxides, i.e., nickel oxide and molybdenum oxide. Overall, both the PCN-RuNPs aptasensor and the PCN-NiMoO<sub>4</sub> NRs aptasensor showed a significantly improved biosensing performance for the quantitative detection of cTn-I. A variety of interactions operate between PCN materials, aptamers, and cTn-I molecules. A biomimetic microenvironment for the incoming aptamers of cTn-I is provided by the N-domains of PCN because of its structural similarity with the N-densities of the nucleotides. The delocalized pi-electrons in the C<sub>3</sub>N<sub>3</sub> rings of the PCN *s*-triazine modules enable pi-stacking interactions with the cTn-I aptamers.

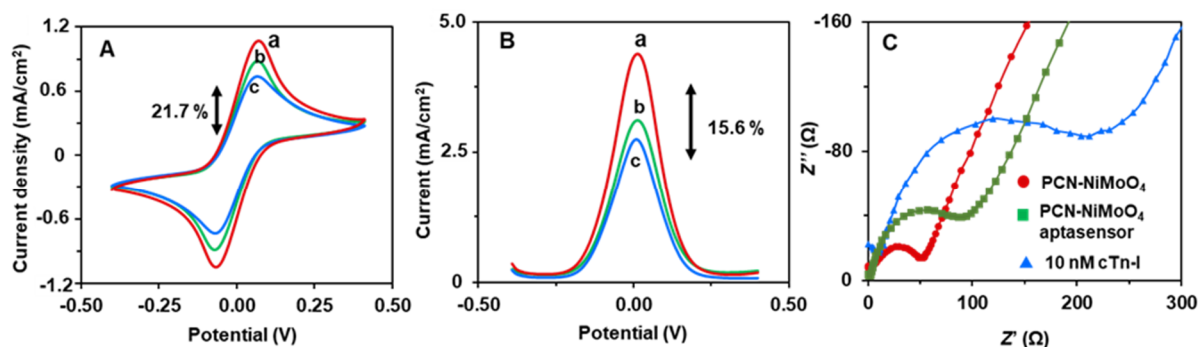


**Figure 7.** (A) CV, (B) SWV, and (C) EIS curves of PCN-NiMoO<sub>4</sub> NPs (a), PCN-NiMoO<sub>4</sub> NPs aptasensor (b), and PCN-NiMoO<sub>4</sub> NPs aptasensor + 10 ng/mL cTn-I (c). The supporting electrolyte 0.10 M KCl containing a mixture of 5.0 mM  $K_3/K_4[Fe(CN)_6]$ .

### 3.4. Determination of cTn-I

Next, quantitative determination of cTn-I was analyzed with the PCN-RuNPs aptasensor and the PCN-NiMoO<sub>4</sub> NRs aptasensor in the presence of various concentrations of cTn-I. The SWV analysis of cTn-I levels was performed, from low nanomolar to high micromolar levels, and their corresponding curves are presented in Figure 8. Both the PCN-RuNPs aptasensor and the PCN-NiMoO<sub>4</sub> NRs aptasensor showed a consistent decrease in the current signal when higher concentrations of cTn-I reacted with the aptamer. Calibration plots were derived by plotting normalized current response against the logarithmic concentration of cTn-I. The PCN-RuNPs aptasensor displayed a linear range of 0.1–10,000 ng/mL, a sensitivity of 0.0579 mA/(ng/mL)/cm<sup>2</sup>, and a detection limit (LOD) of 50 pg/mL. The PCN-NiMoO<sub>4</sub> NRs aptasensor showed a linear range of 0.10–10,000 ng/mL, a sensitivity of 0.0608 mA/(ng/mL)/cm<sup>2</sup>, and a LOD of 70 pg/mL. The sensitivity of the

PCN-NiMoO<sub>4</sub> NRs was slightly better than the PCN-RuNPs, which is due to the slight difference in the background current and signal-to-noise ratio of these two material systems. Overall, both the PCN-RuNPs and PCN-NiMoO<sub>4</sub> NRs aptasensors showed clinically useful analytical parameters. The analytical parameters are comparable with existing cTn-I biosensors (Table 1). In comparison to cTn-I sensors made using conventional electrodes, such as GCE [34] and ITO [35], the use of LSGEs offer several benefits including low-cost, flexibility, mass production, and disposability. However, the synthesis of PCN-RuNPs and PCN-NiMoO<sub>4</sub> NRs depends on multiple lengthy synthesis steps, which is limiting their widespread application. Future research will focus on developing a fast, one-pot synthesis of nanomaterials.

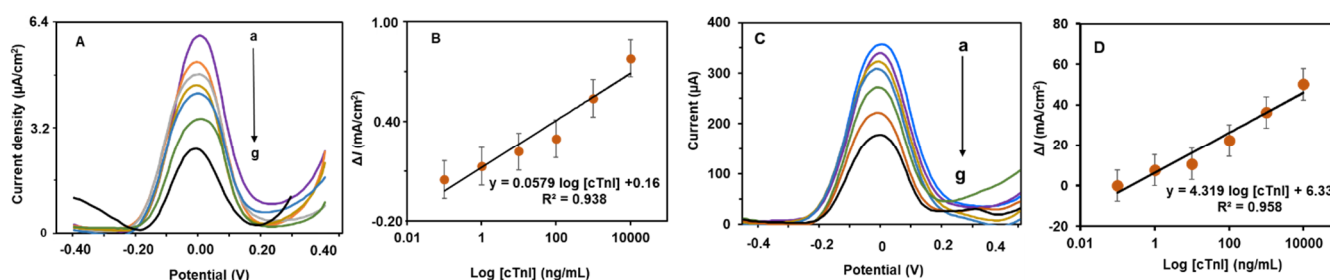


**Figure 8.** (A) SWVs of the PCN-RuNPs biosensor for various concentrations of cTn-I (a = 0, b = 0.1, c = 1.0, d = 10, e = 100, f = 1000, and g = 10,000 ng/mL) and (B) corresponding calibration plot. (C) SWVs of the PCN-NiMoO<sub>4</sub> NRs biosensor for various concentrations of cTn-I (a = 0, b = 0.1, c = 1.0, d = 10, e = 100, f = 1000, and g = 10,000 ng/mL) and (D) corresponding calibration plot.

**Table 1.** Aptasensing performance of PCN-RuNPs and PCN-NiMoO<sub>4</sub> NRs aptasensors in previous reports.

Material	Type	Technique	Linear Range (ng/mL)	LOD (pg/mL)	Real Sample
Porous graphene oxide/GCE [34]	Immunosensor	EIS	0.1–10	70.0	Clinical samples
Zinc ferrite/LSGE [36]	Aptasensor	SWV	0.001–200	1.0	Serum
magnetic metal organic frameworks Fe <sub>3</sub> O <sub>4</sub> @UiO-66/Cu@Au/SPGE [37]	Dual-aptasensor	DPV	0.05–100	16.0	Serum
Manganese oxide-reduced graphene oxide/ITO [35]	Immunosensor	EIS	0.008–20	8.0	Serum
cTnI imprinted polypyrrole/boron nitride quantum dots/GCE [38]	MIP sensor	DPV	0.01–5.00	0.5	Blood serum
Au electrode/Ab <sub>1</sub> (detection probe); HRP-Ab <sub>2</sub> -Au-COF (signal probe) [39]	Sandwich Immunosensor	DPV	0.005–10	1.7	Human serum
PCN-RuNPs/LSGE [this work]	Aptamer	SWV	0.1–10,000	50	Serum
PCN-NiMoO <sub>4</sub> NRs/LSGE [This work]	Aptamer	SWV	0.1–10,000	70	Serum

EIS: Electrochemical impedance spectroscopy; SPGE: Screen-printed gold electrode; Apt: Aptamer; Ab<sub>1</sub>: primary antibody; Ab<sub>2</sub>: Secondary antibody; COF: covalent organic frameworks; MIP: molecularly imprinted polymer.

Next, the selectivity of the PCN-RuNPs and PCN-NiMoO<sub>4</sub> NRs aptasensors was examined in the presence of several potentially interfering biomolecules, including cTnI, cholesterol, myoglobin, and glucose (Figure 9). The normalized responses of the other tested molecules were less than 5%, indicating the appreciable selectivity of the aptasensor. The selectivity nature of the biosensors entirely originated from the specificity of the aptamer sequence that was exclusively made for cTn-I. Next, the reproducibility of the aptasensors was tested. Five PCN-RuNPs aptasensors were prepared individually and their biosensing performance towards cTn-I was tested. The R.S.D. value of these five readings was less than 4.7%, suggesting the acceptable reproducibility of the sensor. Similar results were observed for the reproducibility of five individual PCN-NiMoO<sub>4</sub> NRs aptasensors. Next, the storage stability of the biosensors was tested by recording their cTn-I sensing

performance for a week, one reading per day. The sensors were stored at 4 °C, maintaining a humid environment when not in use. About 91.3% and 89.5% of the initial signal responses were retained after six days of use for the PCN-RuNPs and PCN-NiMoO<sub>4</sub> NRs, respectively, suggesting acceptable stability. The aptamers were effectively attached to the nanomaterial-modified electrode, and the immobilization was consistent between different electrodes, providing stable and reproducible signals on multiple electrodes. The practical utility of the PCN-RuNPs aptasensor and the PCN-NiMoO<sub>4</sub> NRs was demonstrated in human serum samples (Figure 9C–F). Three different quantities of cTn-I were spiked into the serum and the spiked samples were analyzed by SWV. A significant decrease was noted when cTn-I-spiked samples were incubated with the aptasensors. The spiked levels of cTn-I were calculated from the normalized current. Thus, the PCN-RuNPs aptasensor and the PCN-NiMoO<sub>4</sub> NRs aptasensor were found to be practically useful for real-world applications. It is worth mentioning that the use of a disposable LSGE as an electrode holds direct clinical applications [40].

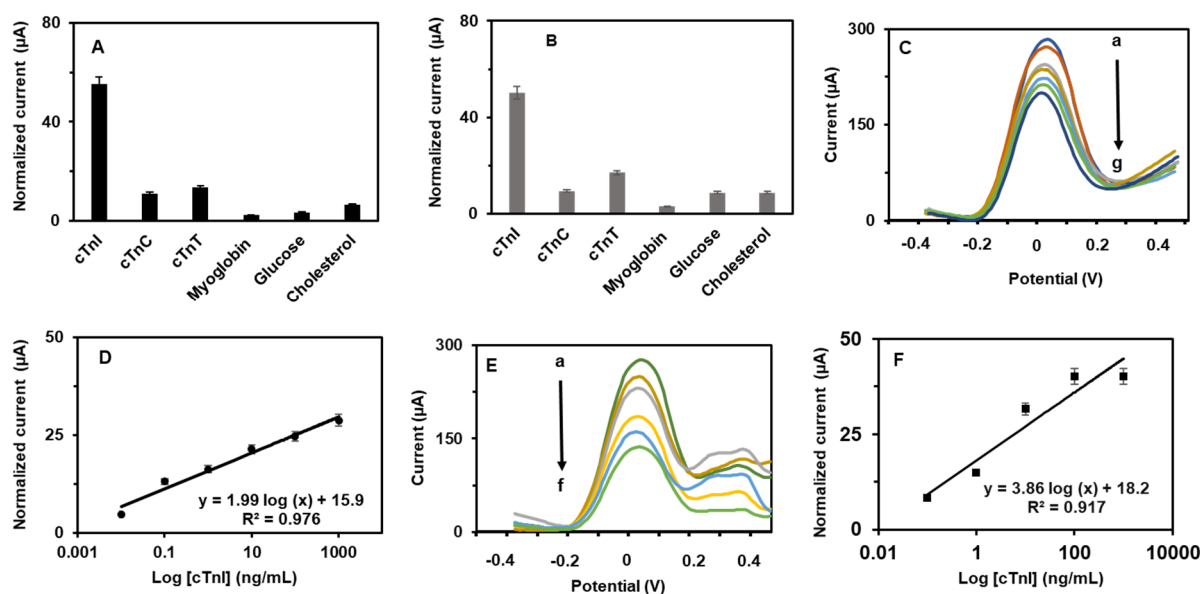


**Figure 9.** (A) Selectivity of PCN-RuNPs aptasensor and (B) PCN-NiMoO<sub>4</sub> NRs aptasensor. SWV responses of 100 pg/mL cTn-I co-existed with 100 pg/mL cTnT, myoglobin, cholesterol, and glucose were recorded. (C,D) Practicality of PCN-RuNPs aptasensor and (E,F) PCN-NiMoO<sub>4</sub> aptasensor in cTn-I-spiked human serum samples; a = 0, b = 0.1, c = 1.0, d = 10, e = 100, and f = 1000 ng/mL cTnI and their calibration plot.

#### 4. Conclusions

Functionalized porous graphitic carbon nitride nanomaterial-based 2D nanocomposites are excellent materials to use in fabricating highly sensitive and selective cTn-I biosensors. The 2D layered structure, porous structure, defect sites, and dopants of the PCN materials are found to be highly relevant for accommodating aptamers and establishing facile aptamer-analyte interactions. PCN-RuNPs and PCN-NiMoO<sub>4</sub> nanomaterials have appreciable surface properties, electrochemically active surface areas, and biosensing properties. Their distinctive microstructures and nanostructures offer locations for immobilizing significant numbers of active aptamers. PCN-RuNPs and PCN-NiMoO<sub>4</sub> aptasensors can detect cTn-I in the wide range of 0.1–10,000 ng/mL. The LOD of cTn-I detection was 70.0 pg/mL for the PCN-RuNPs aptasensor and 50.0 pg/mL for the PCN-RuNPs aptasensor. The sample volume of 10 μL is sufficient for practical analysis, which is useful for analyzing clinical samples. Furthermore, the aptasensors are selective and practically feasible in human serum samples.

**Author Contributions:** Conceptualization, W.K., V.M. and K.N.S.; methodology, W.K.; software, W.K. and K.P.; validation, W.K., V.M., K.P. and K.N.S.; formal analysis, W.K.; investigation, V.M.; resources, K.-W.H. and K.N.S.; data curation, W.K.; writing—original draft preparation, W.K. and V.M.; writing—review and editing, V.M. and K.N.S.; visualization, V.M.; supervision, K.-W.H. and K.N.S.; project administration, V.M.; funding acquisition, K.N.S. All authors have read and agreed to the published version of the manuscript.

**Funding:** This research was funded by King Abdullah University of Science and Technology (KAUST), Thuwal, Saudi Arabia, and KAUST Smart Health Initiative.

**Institutional Review Board Statement:** Not applicable.

**Informed Consent Statement:** Not applicable.

**Data Availability Statement:** Not applicable.

**Conflicts of Interest:** The authors declare no conflict of interest.

## References

1. Surya, S.G.; Majhi, S.M.; Agarwal, D.K.; Lahcen, A.A.; Yuvaraja, S.; Chappanda, K.N.; Salama, K.N. A label-free aptasensor FET based on Au nanoparticle decorated  $\text{Co}_3\text{O}_4$  nanorods and a SWCNT layer for detection of cardiac troponin T protein. *J. Mater. Chem. B* **2020**, *8*, 18–26. [[CrossRef](#)] [[PubMed](#)]
2. Ouyang, M.; Tu, D.; Tong, L.; Sarwar, M.; Bhimaraj, A.; Li, C.; Cote, G.L.; di Carlo, D. A review of biosensor technologies for blood biomarkers toward monitoring cardiovascular diseases at the point-of-care. *Biosens. Bioelectron.* **2021**, *171*, 112621. [[CrossRef](#)] [[PubMed](#)]
3. Savonnet, M.; Rolland, T.; Cubizolles, M.; Roupioz, Y.; Buhot, A. Recent advances in cardiac biomarkers detection: From commercial devices to emerging technologies. *J. Pharm. Biomed. Anal.* **2021**, *194*, 113777. [[CrossRef](#)] [[PubMed](#)]
4. Mani, V.; Durmus, C.; Khushaim, W.; Ferreira, D.C.; Timur, S.; Arduini, F.; Salama, K.N. Multiplexed sensing techniques for cardiovascular disease biomarkers—A review. *Biosens. Bioelectron.* **2022**, *216*, 114680. [[CrossRef](#)]
5. Pourali, A.; Rashidi, M.R.; Barar, J.; Pavon-Djavid, G.; Omid, Y. Voltammetric biosensors for analytical detection of cardiac troponin biomarkers in acute myocardial infarction. *TrAC Trends Anal. Chem.* **2021**, *134*, 116123. [[CrossRef](#)]
6. Bolotsky, A.; Butler, D.; Dong, C.; Gerace, K.; Glavin, N.R.; Muratore, C.; Robinson, J.A.; Ebrahimi, A. Two-dimensional materials in biosensing and healthcare: From in vitro diagnostics to optogenetics and beyond. *ACS Nano* **2019**, *13*, 9781–9810. [[CrossRef](#)]
7. Cai, X.; Luo, Y.; Liu, B.; Cheng, H.-M. Preparation of 2D material dispersions and their applications. *Chem. Soc. Rev.* **2018**, *47*, 6224–6266. [[CrossRef](#)]
8. Kumar, S.; Lei, Y.; Alshareef, N.H.; Quevedo-Lopez, M.A.; Salama, K.N. Biofunctionalized two-dimensional  $\text{Ti}_3\text{C}_2$  MXenes for ultrasensitive detection of cancer biomarker. *Biosens. Bioelectron.* **2018**, *121*, 243–249. [[CrossRef](#)]
9. Zhu, L.; Farhat, M.; Salama, K.N.; Chen, P.-Y. Two-dimensional materials-based radio frequency wireless communication and sensing systems for Internet-of-things applications. In *Emerging 2D Materials and Devices for the Internet of Things*; Elsevier: Amsterdam, The Netherlands, 2020; pp. 29–57.
10. Liao, G.; He, F.; Li, Q.; Zhong, L.; Zhao, R.; Che, H.; Gao, H.; Fang, B. Emerging graphitic carbon nitride-based materials for biomedical applications. *Prog. Mater. Sci.* **2020**, *112*, 100666. [[CrossRef](#)]
11. Rajaji, U.; Chinnapaiyan, S.; Chen, S.-M.; Govindasamy, M.; de Oliveira Filho, J.I.; Khushaim, W.; Mani, V. Design and fabrication of yttrium ferrite garnet-embedded graphitic carbon nitride: A sensitive electrocatalyst for smartphone-enabled point-of-care pesticide (mesotrione) analysis in food samples. *ACS Appl. Mater. Interfaces* **2021**, *13*, 24865–24876. [[CrossRef](#)]
12. Rajaji, U.; Selvi, S.V.; Chen, S.-M.; Chinnapaiyan, S.; Chen, T.-W.; Govindasamy, M. A nanocomposite consisting of cuprous oxide supported on graphitic carbon nitride nanosheets for non-enzymatic electrochemical sensing of 8-hydroxy-2'-deoxyguanosine. *Microchim. Acta* **2020**, *187*, 1–10. [[CrossRef](#)]
13. Li, Y.; Li, X.; Zhang, H.; Xiang, Q. Porous graphitic carbon nitride for solar photocatalytic applications. *Nanoscale Horiz.* **2020**, *5*, 765–786. [[CrossRef](#)] [[PubMed](#)]
14. Wang, C.; Fan, H.; Ren, X.; Fang, J.; Ma, J.; Zhao, N. Porous graphitic carbon nitride nanosheets by pre-polymerization for enhanced photocatalysis. *Mater. Charact.* **2018**, *139*, 89–99. [[CrossRef](#)]
15. Hou, Y.; Yang, J.; Lei, C.; Yang, B.; Li, Z.; Xie, Y.; Zhang, X.; Lei, L.; Chen, J. Nitrogen vacancy structure driven photoelectrocatalytic degradation of 4-chlorophenol using porous graphitic carbon nitride nanosheets. *ACS Sustain. Chem. Eng.* **2018**, *6*, 6497–6506. [[CrossRef](#)]
16. Gupta, N.; Todi, K.; Narayan, T.; Malhotra, B. Graphitic carbon nitride-based nanoplatfoms for biosensors: Design strategies and applications. *Mater. Today Chem.* **2022**, *24*, 100770.
17. Idris, A.O.; Oseghe, E.O.; Msagati, T.A.; Kuvarega, A.T.; Feloni, U.; Mamba, B. Graphitic carbon nitride: A highly electroactive nanomaterial for environmental and clinical sensing. *Sensors* **2020**, *20*, 5743. [[CrossRef](#)] [[PubMed](#)]
18. Liang, Q.; Li, Z.; Yu, X.; Huang, Z.-H.; Kang, F.; Yang, Q.-H. Macroscopic 3D Porous Graphitic Carbon Nitride Monolith for Enhanced Photocatalytic Hydrogen Evolution. *Adv. Mater.* **2015**, *27*, 4634–4639. [[CrossRef](#)]

19. Bhowmik, T.; Kundu, M.K.; Barman, S. Highly active and durable Pd nanoparticles-porous graphitic carbon nitride composite for electrocatalytic oxygen reduction reaction. *Int. J. Hydrogen Energy* **2016**, *41*, 14768–14777.
20. Fischer, A.; Antonietti, M.; Thomas, A. Growth confined by the nitrogen source: Synthesis of pure metal nitride nanoparticles in mesoporous graphitic carbon nitride. *Adv. Mater.* **2007**, *19*, 264–267. [[CrossRef](#)]
21. Rajkumar, C.; Thirumalraj, B.; Chen, S.-M.; Veerakumar, P.; Liu, S.-B. Ruthenium nanoparticles decorated tungsten oxide as a bifunctional catalyst for electrocatalytic and catalytic applications. *ACS Appl. Mater. Interfaces* **2017**, *9*, 31794–31805. [[CrossRef](#)]
22. Gallay, P.; Eguílaz, M.; Rivas, G. Designing electrochemical interfaces based on nanohybrids of avidin functionalized-carbon nanotubes and ruthenium nanoparticles as peroxidase-like nanozyme with supramolecular recognition properties for site-specific anchoring of biotinylated residues. *Biosens. Bioelectron.* **2020**, *148*, 111764. [[CrossRef](#)] [[PubMed](#)]
23. Veerakumar, P.; Hung, S.-T.; Hung, P.-Q.; Lin, K.-C. Review of the design of ruthenium-based nanomaterials and their sensing applications in electrochemistry. *J. Agric. Food Chem.* **2022**, *70*, 8523–8550. [[CrossRef](#)] [[PubMed](#)]
24. Lou, B.-S.; Rajaji, U.; Chen, S.-M.; Chen, T.-W. A simple sonochemical assisted synthesis of NiMoO<sub>4</sub>/chitosan nanocomposite for electrochemical sensing of amlodipine in pharmaceutical and serum samples. *Ultrason. Sonochem.* **2020**, *64*, 104827. [[CrossRef](#)]
25. Jo, H.; Gu, H.; Jeon, W.; Youn, H.; Her, J.; Kim, S.-K.; Lee, J.; Shin, J.H.; Ban, C. Electrochemical aptasensor of cardiac troponin I for the early diagnosis of acute myocardial infarction. *Anal. Chem.* **2015**, *87*, 9869–9875. [[CrossRef](#)] [[PubMed](#)]
26. Rauf, S.; Lahcen, A.A.; Aljedaibi, A.; Beduk, T.; Ilton de Oliveira Filho, J.; Salama, K.N. Gold nanostructured laser-scribed graphene: A new electrochemical biosensing platform for potential point-of-care testing of disease biomarkers. *Biosens. Bioelectron.* **2021**, *180*, 113116. [[CrossRef](#)]
27. Beduk, T.; de Oliveira Filho, J.I.; Ait Lahcen, A.; Mani, V.; Salama, K.N. Inherent Surface activation of laser-scribed graphene decorated with au and ag nanoparticles: Simultaneous electrochemical behavior toward uric acid and dopamine. *Langmuir* **2021**, *37*, 13890–13902. [[CrossRef](#)] [[PubMed](#)]
28. Ghanam, A.; Lahcen, A.A.; Beduk, T.; Alshareef, H.N.; Amine, A.; Salama, K.N. Laser scribed graphene: A novel platform for highly sensitive detection of electroactive biomolecules. *Biosens. Bioelectron.* **2020**, *168*, 112509. [[CrossRef](#)]
29. Hornberger, E.; Bergmann, A.; Schmies, H.; Kühl, S.; Wang, G.; Drnec, J.; Sandbeck, D.J.; Ramani, V.; Cherevko, S.; Mayrhofer, K.J. In situ stability studies of platinum nanoparticles supported on ruthenium–titanium mixed oxide (RTO) for fuel cell cathodes. *ACS Catal.* **2018**, *8*, 9675–9683. [[CrossRef](#)]
30. Cored, J.; García-Ortiz, A.; Iborra, S.; Climent, M.J.; Liu, L.; Chuang, C.-H.; Chan, T.-S.; Escudero, C.; Concepción, P.; Corma, A. Hydrothermal synthesis of ruthenium nanoparticles with a metallic core and a ruthenium carbide shell for low-temperature activation of CO<sub>2</sub> to methane. *J. Am. Chem. Soc.* **2019**, *141*, 19304–19311. [[CrossRef](#)]
31. Oudghiri-Hassani, H.; Al Wadaani, F. Preparation, characterization and catalytic activity of nickel molybdate (NiMoO<sub>4</sub>) nanoparticles. *Molecules* **2018**, *23*, 273. [[CrossRef](#)]
32. Chen, J.; Zhao, G.; Chen, Y.; Rui, K.; Mao, H.; Dou, S.X.; Sun, W. Iron-doped nickel molybdate with enhanced oxygen evolution kinetics. *Chem. Eur. J.* **2019**, *25*, 280–284. [[CrossRef](#)] [[PubMed](#)]
33. Dong, Y.; Wang, Q.; Wu, H.; Chen, Y.; Lu, C.-H.; Chi, Y.; Yang, H.-H. Graphitic carbon nitride materials: Sensing, imaging and therapy. *Small* **2016**, *12*, 5376–5393. [[CrossRef](#)] [[PubMed](#)]
34. Kazemi, S.H.; Ghodsi, E.; Abdollahi, S.; Nadri, S. Porous graphene oxide nanostructure as an excellent scaffold for label-free electrochemical biosensor: Detection of cardiac troponin I. *Mate. Sci. Eng. C* **2016**, *69*, 447–452.
35. Singh, N.; Ali, M.A.; Rai, P.; Sharma, A.; Malhotra, B.; John, R. Microporous nanocomposite enabled microfluidic biochip for cardiac biomarker detection. *ACS Appl. Mater. Interfaces* **2017**, *9*, 33576–33588.
36. Rauf, S.; Mani, V.; Lahcen, A.A.; Yuvaraja, S.; Beduk, T.; Salama, K.N. Binary transition metal oxide modified laser-scribed graphene electrochemical aptasensor for the accurate and sensitive screening of acute myocardial infarction. *Electrochim. Acta* **2021**, *386*, 138489. [[CrossRef](#)]
37. Sun, D.; Luo, Z.; Lu, J.; Zhang, S.; Che, T.; Chen, Z.; Zhang, L. Electrochemical dual-aptamer-based biosensor for nonenzymatic detection of cardiac troponin I by nanohybrid electrocatalysts labeling combined with DNA nanotetrahedron structure. *Biosens. Bioelectron.* **2019**, *134*, 49–56.
38. Yola, M.L.; Atar, N. Development of cardiac troponin-I biosensor based on boron nitride quantum dots including molecularly imprinted polymer. *Biosens. Bioelectron.* **2019**, *126*, 418–424. [[CrossRef](#)]
39. Feng, S.; Yan, M.; Xue, Y.; Huang, J.; Yang, X. Electrochemical immunosensor for cardiac troponin I detection based on covalent organic framework and enzyme-catalyzed signal amplification. *Anal. Chem.* **2021**, *93*, 13572–13579.
40. Beduk, D.; Ilton de Oliveira Filho, J.; Beduk, T.; Harmanci, D.; Zihnioglu, F.; Cicek, C.; Serto, R.; Arda, B.; Goksel, T.; Turhan, K.; et al. ‘All In One’ SARS-CoV-2 variant recognition platform: Machine learning-enabled point of care diagnostics. *Biosens. Bioelectron. X* **2022**, *10*, 100105. [[CrossRef](#)]